A Voltage-supportive Controller for Ultra-fast Electric Vehicle Chargers in Islanded DC Microgrids

Noushin Poursafar, *Student Member*, *IEEE*, Seyedfoad Taghizadeh, M. Jahangir Hossain, *Senior Member*, *IEEE*, and Masoud Karimi-Ghartemani, *Senior Member*, *IEEE*

***Abstract*—This paper presents a controller for fast and ultra-fast electric vehicle (EV) charging stations. Without affecting the charging efficiency, the proposed controller enables the charger to provide support to the interconnection voltage to counter and damp its transients. Existing solutions are either hardware-based such as using supercapacitors and flywheels which increase the cost and bulkiness of the charging station, or software-based such as *P*/*V* droop methods which are still unable to provide a robust and strong voltage support. This paper proposes an emulated supercapacitor concept in the control system of the ultra-fast EV charger in an islanded DC microgrid. Thus, it converts the EV from a static load to a bus voltage supportive load, leading to reduced bus voltage oscillations during single and multiple ultra-fast EV charging operations, and rides through and provides supports during extreme external disturbances. Detailed analysis and design guidelines of the proposed controller are presented, and its effectiveness and improved performance compared with conventional techniques are shown for different case studies.**

***Index Terms*—Electric vehicle (EV), charging station, ultra-fast charging, DC microgrid, voltage support, capacitor emulation.**

I. Introduction

THE replacement of internal combustion engine vehicles with electric vehicles (EVs) is attracting increasing attention from research institutes and industrial sectors. One of the global challenges of EV transportation is their charging time, which can take up to 10 hours using Level-1 and Level-2 charging modes [1]. The charging time can be significantly reduced (down to about one hour) by employing ultra-fast chargers that use Level-3 charging mode [1]. Since the battery capacity of a typical EV is between 20 kWh and 670 kWh [2], ultra-fast charging corresponds to a large load that is almost twenty times that of a typical house [3]. This can cause serious issues such as voltage drops [4], grid equipment overloading [5], [6], and current harmonic distortion [7], [8] for the power grid.

To deal with such challenges, various solutions have been proposed in the existing literature. For example, [9] proposes to connect a large battery to the DC bus of a fast-charging station to support the DC-bus voltage during the charging process. In [10], a super-conducting magnetic energy storage (SMES) system is connected to the DC bus of a fast EV charging station. The use of a flywheel energy storage system (ESS) is proposed in [11]. In [12], a hybrid battery, flywheel, and supercapacitor are used in a DC microgrid (DC-MG) to reduce the transients of the DC-bus voltage. In [13] and [14], a unidirectional 12-pulse diode rectifier is proposed to reduce the oscillations of the DC-bus voltage as well as the harmonics of the AC-bus current. In [15], a battery is used as a buffer between an AC grid and a charging station, where the buffer charges slowly from the power grid and discharges fast to meet the energy demanded by fast EV chargers. The main drawback of this method is the delay caused by charging the buffer before the arrival of the next EV. Such existing solutions are hardware-based approaches that inevitably increase the cost and bulkiness of the charging station.

There are some software-based solutions as well. In [16], a wide-area controller is used for a 12-bus microgrid to minimize voltage fluctuations during the charging of 800 EVs in eight parking lots. It collects the output data of the power system stabilizers of all generators and uses an automatic voltage regulator (AVR) to minimize the grid voltage oscillations via regulating the output power of the generators. This method has the drawbacks of complex data collection and high dependency on the communication network. In [17], a bidirectional EV fast-charging station is proposed to solve the voltage drop problem wherein the EVs are connected to the DC bus through DC/DC converters and can be fast charged using a constant current or reduced current control approach. The DC bus is connected to the AC grid through a 3-phase inverter, which can regulate the DC-bus voltage as well as the AC grid voltage by providing reactive power

Manuscript received: May 24, 2022; revised: September 19, 2022; accepted: October 29, 2022. Date of CrossCheck: October 29, 2022. Date of online publication: January 17, 2023.

N. Poursafar (corresponding author) and S. Taghizadeh are with School of Engineering, Macquarie University, Sydney, NSW 2109, Australia (e-mail:noushin.poursafar@students.mq.edu.au; foad.taghizadeh@mq.edu.au).

M. J. Hossain is with School of Electrical and Data Engineering, University of Technology Sydney, Sydney, NSW 2007, Australia (e-mail: jahangir.hossain@uts.edu.au).

M. Karimi-Ghartemani is with Department of Electrical and Computer Engineering, Mississippi State University, Mississippi, MS 39762, USA (e-mail: karimi@ece.msstate.edu).

DOI: 10.35833/MPCE.2022.000304

compensation and correcting the power factor. However, this method relies on the presence of an AC grid. In [18], the EVs operate as a voltage regulator for the AC microgrid, by providing reactive power, operating as economical solutions compared with capacitor banks and static var compensators. In [19], the reactive power command is generated locally by using Q/V droop control approach. In [20], EV chargers are used for voltage regulation and loss reduction in AC microgrids via managing active and reactive power through some optimization techniques such as genetic algorithm (GA), water cycle algorithm (WCA), and Benders decomposition (BD). The approach of using the P/V droop control method in an EV to improve the balance between generation and load is proposed in [21]. The P/V droop provides a "static" support and has a slow dynamics, while proper selection of its droop coefficient can become a challenge [22], and as we will show in this paper, it is not able to strongly dampen the transients of the DC-bus voltage. To mitigate the drawbacks and limitations of the existing solutions, this paper proposes a software-based method for each EV charger in the charging station. In the proposed controller, the conventional P/V droop control method is neatly combined with a virtual capacitor concept. The result is to turn the EV from a static passive load into a dynamic voltage-supportive load without requiring any additional equipment, i.e., ESS, supercapacitor, SMES. It is shown that compared with existing methods, the proposed method exhibits a faster and stronger DC-bus voltage support without impacting the charging rate. The proposed method is able to reduce the bus voltage oscillations caused by single and multiple ultra-fast charging processes, and extreme external disturbances such as sudden voltage drops in the DCMG. The proposed controller has a simple structure which is analyzed and its parameters are designed systematically in this paper. This paper presents multiple case studies to illustrate the performances of the proposed controller under various conditions.

II. Islanded DCMG Model

The overall configuration of an islanded DCMG with a local charging station is shown in Fig. 1. The DCMG includes four 50 kW PVs (PV_1-PV_4), four 32 kWh battery energy storage systems (BESSs) ($BESS_1$-$BESS_4$), and a local EV charging station. The charging station has three ultra-fast chargers and a local 15 kW PV (PV_5), all of which are connected through a circuit breaker to the 650 V DC bus. SunPower 315 NE series solar panels with 30 strings of five panels are used for 50 kW PVs, and the same model with 10 strings and five panels is used for the 15 kW PV of the charging station. All PVs are connected to buses via DC/DC boost converters that operate in the maximum power point tracking (MPPT) control mode. The solar irradiance profile presented in [23] is used for PV_5 and it is shifted by −1 s, −0.5 s, 0.5 s, and 1 s and applied to PV_1-PV_4, respectively, to create different irradiance patterns for the PVs. The BESSs and EVs are modelled with lithium-ion batteries with 350 V nominal voltage and a rated capacity of 90 Ah. Table I presents the system parameters of the DCMG model.

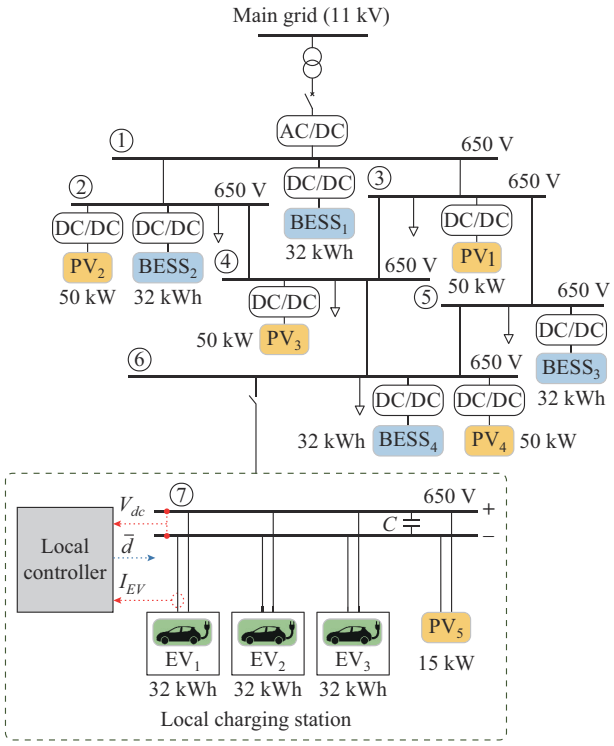

Fig. 1. Configuration of islanded DCMG with a local charging station.

TABLE I
System Parameters of DCMG Model

Circuit parameter	Item	Value
L_p	Inductance of PV converter	5 mH
L_b	Inductance of EV/BESS converter	5 mH
C	DC-bus capacitor	4 mF
f_{sw}	Switching frequency of converter pulse width modulation (PWM)	20 kHz
t_{samp}	Simulation sampling time	1 μs

All the BESSs and PVs use the conventional control methods presented in [23]-[25]. The EV charger, which is the focus of this paper, uses the proposed method. The role of the BESS is to maintain the local DC-bus voltage at a desired value of 650 V. In the BESS controller presented in [24], the proportional gain and integral gain of the BESS current controller are set at $K_{PH}=0.01$ and $K_{IH}=1$, respectively; and the proportional gain and integral gain of the BESS voltage controller are set at $K_{PC}=0.8$ and $K_{IC}=40$, respectively, to achieve a closed loop response with a settling time of 0.1 s and overshoot of below 5% for the load variations of $R=10\,\Omega$ and $R=100\,\Omega$, respectively. The MPPT control algorithms presented in [23] and [25] are used for all PVs with the MPPT proportional gain K_{PP} and the MPPT integral gain K_{IP} set to be 0.0001 and 0.007, respectively.

III. Proposed Controller for EV Charger

This section investigates the alternatives for the local controller of the ultra-fast EV charger shown in Fig. 1, where no additional hardware (i. e., supercapacitors, SMES, flywheels, etc.) is used. Three control methods are presented:

① a conventional current control (CC method), where the EV becomes a static/passive load, as shown in Fig. 2(a); ② a conventional current control with droop-based strategy (CCD method), as shown in Fig. 2(b); and ③ the proposed current control with droop and capacitor emulation (CCDCE method), as shown in Fig. 1(c). The last two turn the EV to a bus voltage supportive load but with different dynamics. The three control methods for EV charging are shown in Fig. 2.

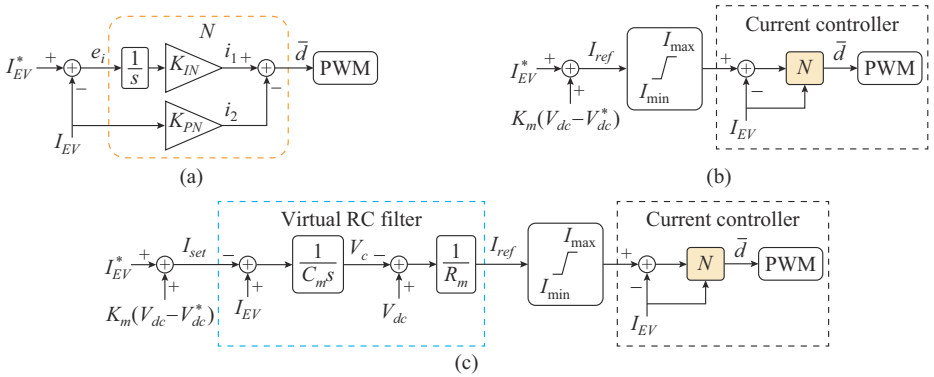

Fig. 2. Three different control methods for EV charging. (a) CC method. (b) CCD method. (c) CCDCE method.

The CC method is a common controller that is used to charge an EV in charging stations with the desired current I_{EV}^*. In this method, the control command $\bar{d}$ shown in Fig. 2(a) is generated by using the PI controller N. Note that the proportional gain operates on the EV current I_{EV}, not on the error e_i. This allows direct application of the optimal state feedback tools such as an optimal method called linear quadratic regulator (LQR) and it achieves improvement in the transient response. This would be explained in Section III-A.

The CCD method, as shown in Fig. 2(b), uses an additional droop term $K_m(V_{dc}-V_{dc}^*)$, where K_m is droop gain, V_{dc} is the DC-bus volatge, and V_{dc}^* is the desired voltage. The CCD controller changes the EV from a constant-current (static/passive) load to a bus voltage supportive load that can contribute to support the bus voltage while charging the EV. In this method, a limiter is used before the current controller to limit the charging current to an acceptable range. $I_{\max}$ and $I_{\min}$ are the maximum and minimum currents of the limiter, respectively.

The proposed CCDCE method, as shown in Fig. 2(c), neatly adds a virtual RC filter to the CCD method. The RC filter, along with the desired charging current I_{EV}^* and a droop term of the DC-bus voltage error $K_m(V_{dc}-V_{dc}^*)$, generates a reference signal I_{ref} for the inner current controller. This method is an enhanced version of the CCD method that changes an EV from a static bus voltage supportive load to a dynamic bus voltage supportive load. In the CCD method, only a droop term $K_m(V_{dc}-V_{dc}^*)$ is used to generate the reference signal I_{ref}, while in the CCDCE method, the EV responds to the derivative of the DC-bus voltage as well according to the analysis and discussion given below.

To better understand the proposed method, we notice that since the current control loop is fast, I_{EV} is close to I_{ref} within the timescale of voltage transients. Therefore, the virtual RC filter in Fig. 2(c) establishes $I_{set}=I_{EV}^*+K_m(V_{dc}-V_{dc}^*)$, $V_{dc}-V_c=R_mI_{ref}\approx R_mI_{EV}$, and $I_{EV}-I_{set}=C_m\dot{V}_c$, where R_m and C_m are the control parameters of the virtual RC filter; V_c is the voltage of the RC filter; and $\dot{V}_c$ is the derivative of V_c. Meanwhile, since I_{EV} is an inductor current and is continuous, the variable V_c will copy the dynamics of V_{dc}. Therefore, $I_{EV}=I_{set}+C_m\dot{V}_c\approx I_{set}+C_m\dot{V}_{dc}$. In other words, the charger responds to the rate of change of the DC bus voltage, hence a fast dynamic support similar to the inertia response of rotating machines. This behavior is equivalent to adding a capacitor C_m in the charger, i. e., the controller emulates a capacitor, as confirmed by the the circuit model of the proposed CCDCE method shown in Fig. 3. This equivalent circuit model is derived based on the above discussion. In the following sections, the design procedure of each individual control method presented in Fig. 3 is explained.

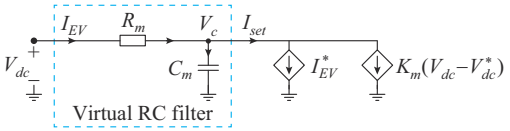

Fig. 3. Equivalent circuit model of proposed CCDCE method.

A. Optimal Design of Gains in CC Method

This subsection presents an optimal design of gains in CC method, which are used in all three controllers. The closed-loop linear time-invariant (LTI) model of Fig. 2(a) is redrawn in Fig. 4.

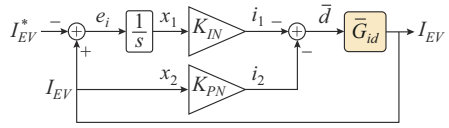

Fig. 4. Closed-loop LTI model of CC method.

In Fig. 4, $\bar{G}_{id}$ is the transfer function between the EV current and the duty cycle given by:

$$\bar{G}_{id}=\frac{I_{EV}}{\bar{d}}=\frac{V_{dc}}{L_bs} \tag{1}$$

Based on the control model presented in Fig. 4 and using (1), the state space representation of the system is expressed as:

$$\begin{cases} \dot{x}_1 = e_i = x_2 - I_{EV}^* \\ \dot{x}_2 = \dfrac{V_{dc}}{L_b}\bar{d} \end{cases} \tag{2}$$

The LQR method is used to achieve the optimal design of the control parameters K_{IN} and K_{PN} [26]. To do so, the model presented by (2) is transformed to a model that can be recognised by the LQR method. By applying the operator d/dt to both sides of (2), we can obtain:

$$\begin{cases} \dot{z}_1 = z_2 \\ \dot{z}_2 = \dfrac{V_{dc}}{L_p} w \end{cases} \tag{3}$$

where $z_1 = \dot{x}_1$; $z_2 = \dot{x}_2$; and $w = \dot{\bar{d}}$. From Fig. 4, the duty cycle $\bar{d}$ is equal to $\bar{d} = -K_{IN}x_1 - K_{PN}x_2 = -\boldsymbol{K}\boldsymbol{x}$. Therefore, w becomes $w = -K_{IN}z_1 - K_{PN}z_2 = -\boldsymbol{K}\boldsymbol{z}$. Therefore, the control block diagram of Fig. 4 can be replaced by the LTI model shown in Fig. 5, where $\boldsymbol{A} = \begin{bmatrix} 0 & 1 \\ 0 & 0 \end{bmatrix}$, $\boldsymbol{B} = \begin{bmatrix} 0 \\ \dfrac{V_{dc}}{L_p} \end{bmatrix}$.

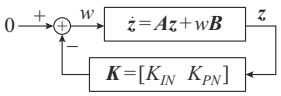

Fig. 5. Control block diagram of CC method using (3).

This model is fully controllable and the LQR is used to minimize the function:

$$J = \int_0^\infty (q_1 z_1^2 + q_2 z_2^2 + w^2)\,\mathrm{d}t = \int_0^\infty (\boldsymbol{z}^{\mathrm{T}}\boldsymbol{Q}\boldsymbol{z} + w^2)\,\mathrm{d}t \tag{4}$$

where $\boldsymbol{Q} = \mathrm{diag}([q_1, q_2])$.

Then, the state feedback vector $\boldsymbol{K}$ is obtained by using the *lqr* command in MATLAB: $\boldsymbol{K} = lqr(\boldsymbol{A}, \boldsymbol{B}, \boldsymbol{Q}, 1)$. Notice that $z_1 = e_i$ and $z_2 = \mathrm{d}I_{EV}/\mathrm{d}t$. By including z_2 into the cost function J, the derivative of the EV current is reduced.

Using the system parameters presented in Table I and $V_{dc} =$ 650 V, the locus of the closed-loop poles (eigenvalues of $\boldsymbol{A} - \boldsymbol{B}\boldsymbol{K}$) is shown in Fig. 6. The blue lines show the effect of increasing q_1 on the placement of the closed-loop poles while q_2 is constant and the red lines show the effect of increasing q_2 when q_1 is constant. As shown in Fig. 6, when $[q_1, q_2] = [0, 0]$, two closed-loop poles are located in A_0.

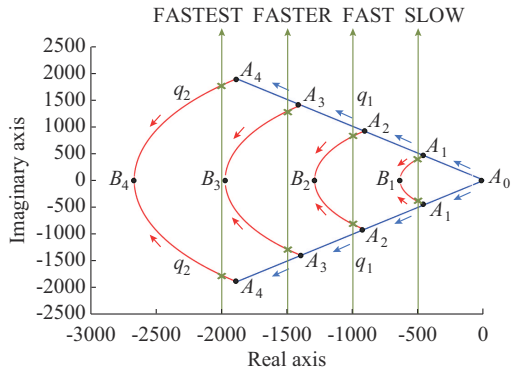

Fig. 6. Closed-loop poles when q_2 is constant and q_1 increases, and when q_1 is constant and q_2 increases.

By keeping $q_2 = 0$ and increasing q_1 to 10, the closed-loop poles move to A_1. Then, by keeping q_1 fixed at 10 and increasing q_2 to 5×10^{-5}, the closed-loop poles move to B_1. Table II presents the corresponding q_1 and q_2 of closed-loop poles are shown with A_0-A_4 and B_1-B_4 in Fig. 6.

TABLE II
CORRESPONDING q_1 AND q_2 OF CLOSED-LOOP POLES

Location of closed-loop poles	$[q_1, q_2]$	Location of closed-loop poles	$[q_1, q_2]$
A_0	$[0, 0]$	B_1	$[10, 0.5 \times 10^{-4}]$
A_1	$[10, 0]$	B_2	$[165, 2.0 \times 10^{-4}]$
A_2	$[165, 0]$	B_3	$[900, 4.5 \times 10^{-4}]$
A_3	$[900, 0]$	B_4	$[3000, 8.5 \times 10^{-4}]$
A_4	$[3000, 0]$		

Based on the effects of q_1 and q_2 on the locations of the closed-loop poles, four different settings of q_1 and q_2 are presented in the following to obtain different locations for the closed-loop poles and consequently to design four controllers with different speeds in terms of tracking the reference signal.

In the SLOW design, the desired real term of the closed-loop poles is −500. To achieve this, q_1 and q_2 are set to be 10 and 1.1×10^{-5}, respectively, and the state-feedback gain is obtained as $\boldsymbol{K} = [3.15, 0.01]$. To shift the closed-loop poles further from the auxiliary axis and have a FAST design, 165 and 4×10^{-5} are selected for q_1 and q_2, respectively. As a result, the closed-loop poles are shifted to $-1000 \pm$ j820 with state-feedback gain of $\boldsymbol{K} = [12.85, 0.01]$. In the FASTER design, q_1 and q_2 are set to be 900 and 7×10^{-5}, respectively, and the state-feedback gain is obtained as $\boldsymbol{K} = [30, 0.02]$. This design relocates the closed-loop poles of the current controller to $-1500 \pm$ j1290 and makes the response of the controller faster. For the FASTEST design, which aims to have the quickest response, q_1 is increased to 3000 and 1.04×10^{-4} is selected for q_2 to place the closed-loop poles at $-2000 \pm$ j1770. In this design, the state-feedback gain is achieved by $\boldsymbol{K} = [54.8, 0.03]$. The locations of the closed-loop poles for each design are shown in Fig. 6 using a green color, and the results of the four designs are summarized in Table III.

TABLE III
FOUR DESIGNS OF CURRENT CONTROLLER N

Design	Pole place	$[q_1, q_2]$	$[K_{IN}, K_{PN}]$
SLOW	$-500 \pm$ j400	$[10, 1.10 \times 10^{-5}]$	$[3.15, 0.01]$
FAST	$-1000 \pm$ j820	$[165, 4.00 \times 10^{-5}]$	$[12.85, 0.01]$
FASTER	$-1500 \pm$ j1290	$[900, 7.00 \times 10^{-5}]$	$[30.00, 0.02]$
FASTEST	$-2000 \pm$ j1770	$[3000, 1.04 \times 10^{-4}]$	$[54.80, 0.03]$

The proposed method can be adjusted and used for different types of the DC/DC converters including the isolated topologies, e. g., the dual active bridge (DAB) converter. In case of having a different topology, the transfer function G_{id}

in (1) needs to be updated, and then the control parameters are selected based on the design procedure explained in this section.

To find the best design for the current controller N, the following tests are conducted.

1) Test A: Current Reference Tracking

The aim of this test is to compare the speed of four designed current controllers in tracking the reference signal (desired EV charging current). In this test, the EV is initially charged at −90 A. At $t=0.5$ s, the charging current changes from −90 A to −130 A. As shown in Fig. 7, if the FASTEST design is used, a settling time of $t_s=0.003$ s and 4% undershoot are achieved; whereas using the SLOW design, the settling time increases to $t_s=0.017$ s and the undershoot decreases to 2%.

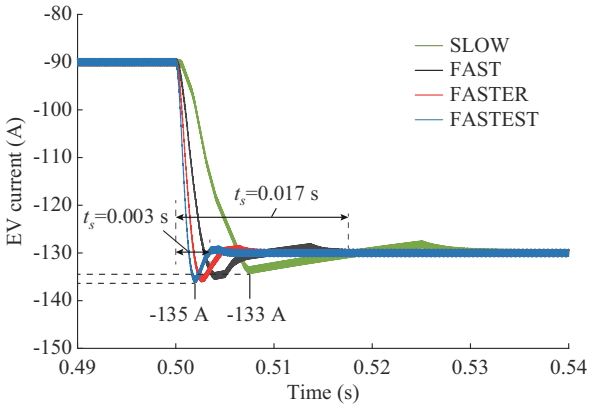

Fig. 7. Test A: dynamic of EV current by using different designs.

2) Test B: Transient Response to Sudden Changes of DC-bus Voltage

At $t=1.0$ s, the DC-bus voltage is manually reduced by −150 V from 650 V and returned to its normal value (650 V) at $t=1.03$ s. Figure 8 shows the dynamic of the EV current during these transitions while comparing the operations of the four designs. As shown in Fig. 8, by using the SLOW design, the EV current experiences ±25 A overshoot/undershoot at step changes of the DC-bus voltage. This value decreases to ±12 A if the FAST design is used; while using the FASTER and FASTEST designs, the overshoot/undershoot of the EV current are further reduced to ±8 A and ±6 A, respectively.

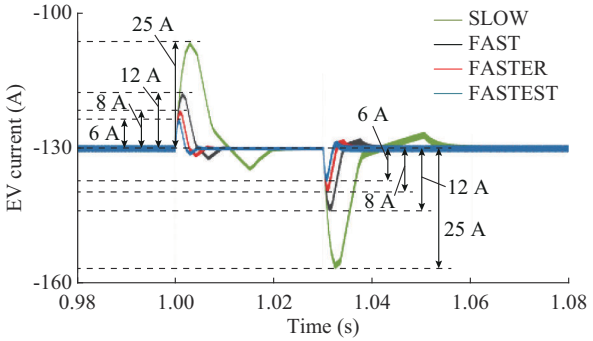

Fig. 8. Test B: dynamic of EV current during DC-bus voltage drop by ±150 V.

Based on these tests, the FASTER and the FASTEST designs provide low undershoot/overshoot on the EV current. However, since shifting the closed-loop poles to be far from the imaginary axis makes the control systems more sensitive to delays and noises in the system, the FASTER design with the closed-loop pole located at $-1500\pm j1290$ is selected as the best design for the inner current controller N. This design is used for the rest of the analysis in this paper. In all control methods, a limiter is used before the current controller to limit the EV current to an acceptable range. The maximum and minimum currents of the limiter are set to be $I_{\max}=100$ A and $I_{\min}=-300$ A, respectively.

B. Design of CCD Method

The same design process for the inner current controller N used in the CC method, presented in Section III-A, is used to design the current controller of the CCD method. The design of the droop controller K_m is done according to the following guideline. Increasing the droop gain K_m could improve the effect of the EV charger on supporting the bus voltage. However, if K_m is too large, the disturbances of the DC-bus voltage are significantly sensed by the inner current control loop. For instance, a small oscillation in the DC-bus voltage causes a large fluctuation in the charging current and can eventually make the system unstable. In this paper, a 1% voltage drop in the DC-bus voltage corresponding to a 20% increase in the EV current is selected as a desired range. Therefore, by using $K_m\cdot(0.01V_{dc}^*)=0.2I_{EV}^*$, the droop gain is calculated as $K_m=20\dfrac{I_{EV}^*}{V_{dc}^*}=20\times\dfrac{130}{650}=4$.

C. Design of CCDCE Method

The design procedure presented in Section III-A is used to design the inner current controller N of the proposed method. The same design process for selecting the droop gain K_m in Section III-B, which is used in the CCD method, is used to design K_m of the proposed method. The design of the virtual RC filter is done according to the following guidelines.

The response of the outer RC filter control loop must be slower than the inner current control loop. While ensuring that the current controller is fast enough according to the design procedure presented in Section III-A, we can assume that $I_{EV}\approx I_{ref}$. As a result, the proposed method in Fig. 2(c) can be simplified to the LTI model shown in Fig. 9.

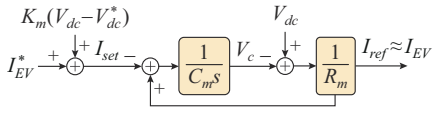

Fig. 9. Simplified model of proposed method shown in Fig. 2(c).

Therefore, the transfer function between I_{ref} ($I_{ref}\approx I_{EV}$) and I_{set} is $1/(\tau_m s+1)$ with its time constant $\tau_m=R_mC_m$. In this paper, the RC parameters are selected such that this time constant is 0.05 s, i.e., sufficiently larger than the current loop time constant. Moreover, C_m is selected large enough to provide adequate damping (or inertia): $C_m\dot{V}_c$ or $C_m\dot{V}_{dc}$. For the desired variation rate of V_{dc} equal to 50 V/s, and to set the variation rate of I_{EV} to be 50 A, C_m is calculated as 0.5 F.

Now setting R_m at 0.1 Ω, the closed-loop pole of the RC filter will be placed at –20.

Finally, Table IV summarizes the control parameters of the BESS, PV, and EV control loops.

TABLE IV
CONTROL PARAMETERS OF BESS, PV, AND EV CONTROL LOOPS

Device	Controller type	Control parameters
BESS	Current controller H	$K_{PH}=0.01$, $K_{IH}=1$
	Voltage controller C	$K_{PC}=0.8$, $K_{IC}=40$
PV	Voltage controller P	$K_{PP}=0.0001$, $K_{IP}=0.007$
EV	Current controller N	$K_{PN}=0.02$, $K_{IN}=30$
	Droop controller	$K_m=4$
	Virtual RC filter	$R_m=0.1\,\Omega$, $C_m=0.1\,F$

IV. STABILITY ANALYSIS OF PROPOSED CONTROLLER

In this section, a stability analysis for the proposed controller is presented. Figure 10 shows an equivalent circuit model of the DCMG and EV charger.

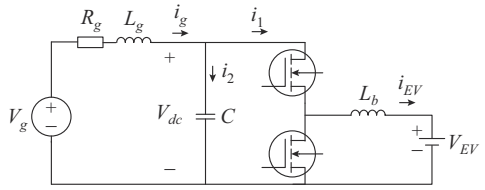

Fig. 10. Equivalent circuit model of DCMG and EV charger.

The dynamic equations of this circuit model are given by:

$$\begin{cases} L_b \dfrac{\mathrm{d}}{\mathrm{d}t} I_{EV} = DV_{dc} - V_{EV} \\ V_g - V_{dc} = R_g I_g + L_g \dfrac{\mathrm{d}}{\mathrm{d}t} I_g \\ C \dfrac{\mathrm{d}}{\mathrm{d}t} V_{dc} = I_g - DI_{EV} \end{cases} \tag{5}$$

where R_g and L_g are the resistance and inductance of the DCMG model, respectively; V_g is the DCMG voltage; V_{EV} is the EV voltage; and D is the duty cycle of the EV charger. After linearizing (5) at $(V_{dc}^*, I_{EV}^*, I_g^*, V_{EV}^*, V_g^*, D^*)$, (5) can be written as:

$$\begin{cases} L_b \dfrac{\mathrm{d}}{\mathrm{d}t} \hat{i}_{EV} = V_{dc}^* D^* - V_{EV}^* + \hat{v}_{\mathrm{dc}} D^* + V_{dc}^* \hat{d} \\ V_g^* - V_{dc}^* - \hat{v}_{dc} = R_g I_g^* + R_g \hat{i}_g + L_g \dfrac{\mathrm{d}}{\mathrm{d}t} \hat{i}_g \\ C \dfrac{\mathrm{d}}{\mathrm{d}t} \hat{v}_{\mathrm{dc}} = I_g^* - I_{EV}^* D^* + \hat{i}_g - (\hat{i}_{EV} D^* + I_{EV}^* \hat{d}) \end{cases} \tag{6}$$

where $\hat{v}_{dc}$, $\hat{i}_{EV}$, $\hat{i}_g$, and $\hat{d}$ are the small AC variations of V_{dc}, i_{EV}, i_g and d, respectively. After eliminating the constant terms of (6), which are equal on both sides at the equilibrium point, (6) can be written in frequency domain as:

$$\begin{cases} -D^* \hat{V}_{dc}(s) + L_b s \hat{I}_{EV}(s) = V_{dc}^* \hat{D}(s) \\ \hat{V}_{dc}(s) + R_g \hat{I}_g(s) + L_g s \hat{I}_g(s) = 0 \\ Cs \hat{V}_{dc}(s) + D^* \hat{I}_{EV}(s) - \hat{I}_g(s) = -I_{EV}^* \hat{D}(s) \end{cases} \tag{7}$$

where $\hat{V}_{dc}(s)$, $\hat{I}_{EV}(s)$, $\hat{I}_g(s)$, and $\hat{D}(s)$ are the Laplace transforms of $\hat{v}_{dc}$, $\hat{i}_{EV}$, $\hat{i}_g$, and $\hat{d}$, respectively. Then, (7) can be written in matrix format as:

$$\boldsymbol{EX}(s) = \boldsymbol{H}\hat{D}(s) \tag{8}$$

where $\boldsymbol{E} = \begin{bmatrix} -D^* & L_b s & 0 \\ 1 & 0 & R_g + sL_g \\ Cs & D^* & -1 \end{bmatrix}$; $\boldsymbol{X}(s) = \begin{bmatrix} \hat{V}_{dc}(s) \\ \hat{I}_{EV}(s) \\ \hat{I}_g(s) \end{bmatrix}$; and $\boldsymbol{H} = \begin{bmatrix} V_{dc}^* \\ 0 \\ -I_{EV}^* \end{bmatrix}$.

Besides, from the LTI model of the proposed controller presented in Fig. 2(c), we have:

$$\begin{cases} \hat{D}(s) = \dfrac{K_{IN}}{s} \hat{I}_{ref}(s) - \left(K_{PN} + \dfrac{K_{IN}}{s} \right) \hat{I}_{EV}(s) \\ \hat{I}_{ref}(s) = \dfrac{1}{R_m} (-\hat{V}_c(s) + \hat{V}_{dc}(s)) \\ \hat{V}_c(s) = \dfrac{1}{C_m s} \hat{I}_{EV}(s) - \hat{I}_{set}(s) \\ \hat{I}_{set}(s) = K_m \hat{V}_{dc}(s) \end{cases} \tag{9}$$

So, the duty cycle of the EV converter in frequency domain, i.e., $\hat{D}(s)$, is equal to:

$$\hat{D}(s) = \frac{K_{IN}(C_m s + K_m)\hat{V}_{dc}(s) - [K_{PN}\tau_m s^2 + K_{IN}(\tau_m s + 1)]\hat{I}_{EV}(s)}{\tau_m s^2} \tag{10}$$

In the matrix form, it is expressed as:

$$\hat{D}(s) = \boldsymbol{F}\boldsymbol{X}(s) \tag{11}$$

where $\boldsymbol{F} = \dfrac{1}{\tau_m s^2} [F_{11}, F_{12}, F_{13}]$, $F_{11} = K_{IN}(C_m s + K_m)$, $F_{13} = 0$, and $F_{12} = -(K_{PN}\tau_m s^2 + K_{IN}(\tau_m s + 1))$.

Substituting (11) into (8) results in $\boldsymbol{EX}(s) = \boldsymbol{HFX}(s)$ or $(\boldsymbol{E} - \boldsymbol{HF})\boldsymbol{X}(s) = \boldsymbol{0}$. Therefore, by solving $|\boldsymbol{E} - \boldsymbol{HF}| = 0$, the closed-loop poles of the proposed controller can be found. Trajectories of the three dominant roots of $|\boldsymbol{E} - \boldsymbol{HF}|$ are shown in Fig. 11 while R_g changes from 0 to 0.5 Ω and L_g changes from 0 to 3 mH. Besides, the system and control parameters in Tables I and IV are used. The variation regions of R_g and L_g are selected based on estimating the microgrid impedance $Z_g = R_g + \mathrm{j}L_g$, where $\vec{Z}_g = -\Delta\vec{v}_{dc}/\Delta\vec{i}_g$ [27]. By considering different load-generation conditions for the microgrid, Z_g is obtained as $(0.5 + \mathrm{j}0.003)\Omega$. As shown in Fig. 11, for all combinations of R_g and L_g, the roots of $|\boldsymbol{E} - \boldsymbol{HF}|$ (the closed-loop poles of the proposed controller) are located in the left half plane, which ensures the stability of the proposed controller.

Figure 12 shows the effect of changing control parameters R_m, C_m, and K_m on the trajectory of the closed-loop pole for both the minimum and maximum values of R_g and L_g (R_g= 0 Ω, $L_g = 0$ mH and $R_g = 0.5\,\Omega$, L_g=3 mH, respectively).

By increasing R_m and C_m, the dominant pole of the closed-loop controller moves to the right. As a result, the closed-loop system becomes slower. In addition, when K_m increases, the dominant pole of the controller is shifted toward left, which makes the closed-loop controller faster.

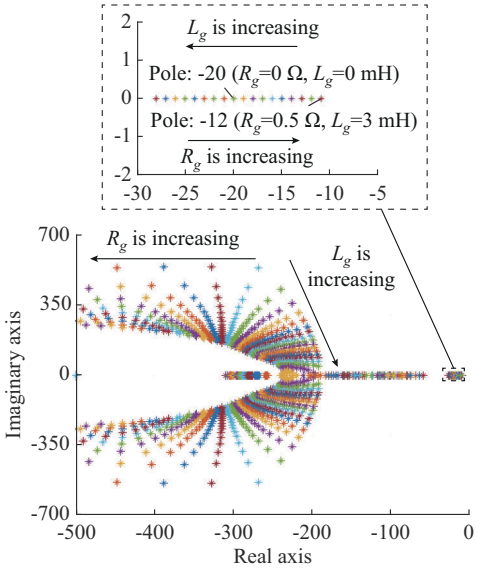

Fig. 11. Trajectories of three dominant roots when R_g and L_g change.

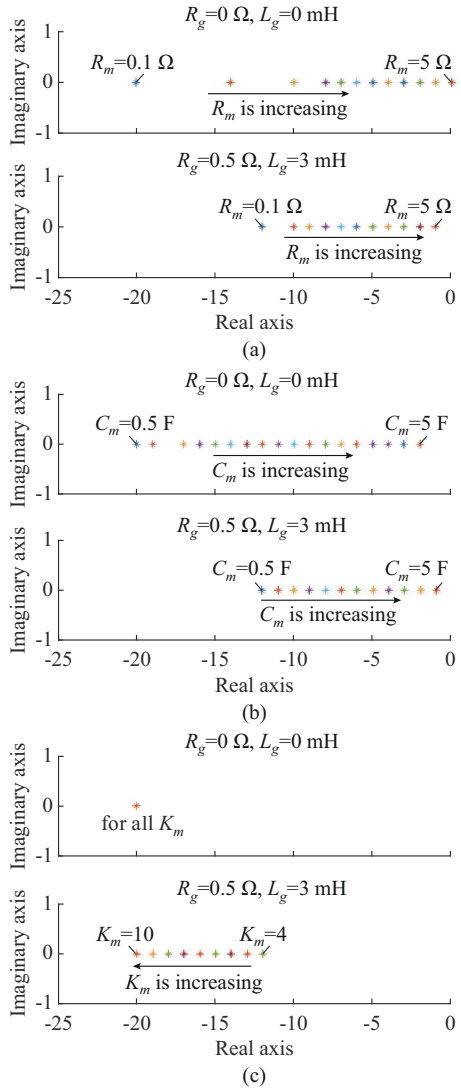

Fig. 12. Loci of dominant roots of $|\boldsymbol{E}-\boldsymbol{HF}|$ for R_g=0 Ω, L_g=0 mH and R_g=0.5 Ω, L_g=3 mH and different values of R_m, C_m, and K_m. (a) R_g is between 0.1 to 5 Ω. (b) C_m is between 0.5 to 5 F. (c) K_m is between 4 to 10.

As can be observed, for variations of all the three control parameters (R_m, C_m, and K_m), the dominant pole of the system remains in the left half plane, which ensures the stability of the system using the proposed method.

V. Results and Discussion

In this section, the control methods presented in Fig. 2 are used for charging EV_1 at the local charging station of the islanded DCMG model (as shown in Fig. 1), and their performances are compared in different case studies as follows: ① testing the dynamic response of the controllers during the ultra-fast charging of EV_1 with the desired charging current of −130 A; ② testing the robustness of the controllers against the presence of high external disturbance including a line-to-ground fault in the DCMG; ③ analyzing the dynamic response of the controllers in a charging station including three ultra-fast EV chargers. It should be mentioned that all case scenarios are conducted in constant current charging region of the battery, where the battery sate of charge (SoC) is from 20% to 80%. In addition, lithium-ion batteries used for EVs are suitable for frequent ultra-fast charging process and the charging current can be increased by twice the rated capacity of the battery (2C) with small impact on the lifetime of batteries [28], [29]. In all cases, the criterion of the DC-bus voltage variation is to follow the standard limit, e. g., ±6%, as recommended by the Australian Renewable Energy Agency [30].

A. Case Study A: Charging an EV with Different Controllers

1) Case Study A1: Comparison of Software-based Solutions

This case study inspects and compares the effects of all charging control methods presented in Fig. 2 on the dynamics of the DC-bus voltage V_{dc} and the current of EV_1. The desired charging current for EV_1 is I_{EV}^*=−130 A. The negative sign of I_{EV}^* shows the charging state, and the positive sign shows the discharging state. Figure 13 presents the dynamics of the DC-bus voltage and EV current. As can be observed in Fig. 13(a), the CC method causes an undershoot of 16% in the DC-bus voltage, which is out of the standard range ±6%, and may activate the protection system and cause an undesired shutdown in the DCMG. On the contrary, when using the CCD and CCDCE methods, EV_1 becomes a static bus voltage supportive load and a dynamic bus voltage supportive load, respectively, and the responses are improved. The CCD and CCDCE methods can regulate the DC-bus voltage V_{dc} in the standard limit (±6% of nominal value) [30] with 3% and 1% undershoots, respectively. This case study shows that the fine control of EV (in the milliseconds range without compromising the charging process) could significantly reduce the undershoot of the DC-bus voltage.

2) Case Study A2: Comparison of Hardware-based Solution and Proposed Software-based Solution

In case study A1, the proposed controller is compared with two software-based methods and its enhanced performance in terms of the DC-bus voltage support is validated. As shown in case study A1, when the CC method is solely used, the DC-bus voltage experiences a high transient during fast charging operation.

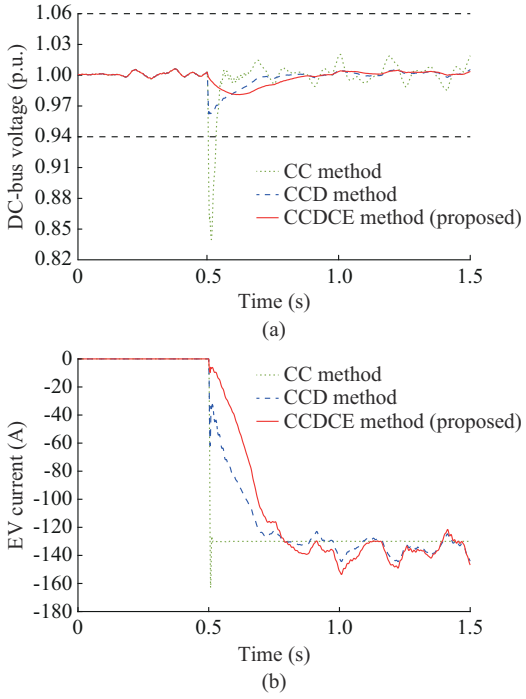

Fig. 13. Case study A1: dynamics of DC-bus voltage and EV current. (a) DC-bus voltage. (b) EV current.

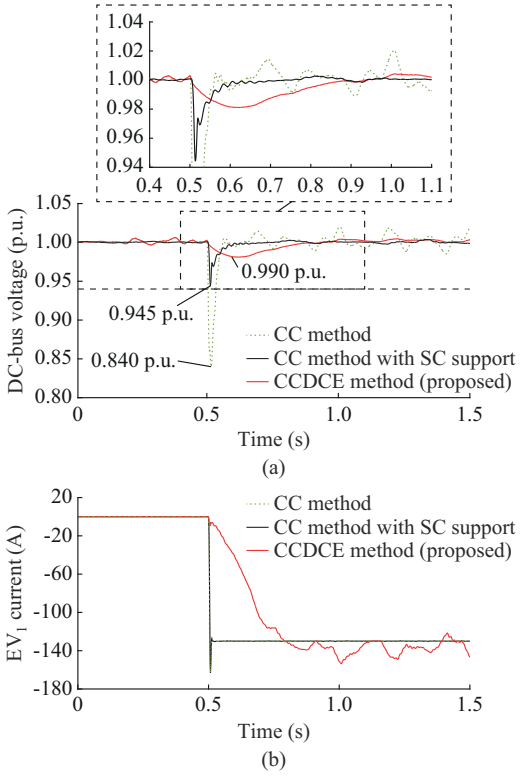

Fig. 14. Case study A2: charging EV_1 with I^*_{EV}=−130 A. (a) DC-bus voltage. (b) EV_1 current.

In one conventional approach, an external (hardware) supercapacitor is used to reduce the oscillations of the DC-bus voltage [31]. In this case study, EV fast charging process is shown while using both the proposed CCDCE method and CC method with a 60 F/350 V supercapacitor connected to bus 7 through a DC/DC converter. The supercapacitor controlled by the same control system is used for the BESS, while the EV uses the CC method. This supercapacitor can provide a constant current of 40 A for the duration of 5 min. The capacity of supercapacitor C_{SC} satisfies $0.5C_{SC}V^2_{SC}=V_{SC}i_{SC}t_{SC}$, where V_{SC} is the voltage of the supercapacitor; i_{SC} is the discharging current; and t_{SC} is the discharging duration.

As shown in Fig. 14(a), when the conventional supercapacitor is used, the DC-bus voltage experiences a 5.5% undershoot (down from 16% of that without using a supercapacitor). However, if the proposed CCDCE method is used, the undershoot of the DC-bus voltage is reduced to 1%, which illustrates the effectiveness of the proposed method compared with the costly hardware-based method.

B. Case Study B: Line-to-ground Fault

This case study investigates the dynamic response of the three control methods (CCDCE, CCD, and CC with SC support) during the presence of a line-to-ground fault in the DCMG. At $t=1.5$ s, a line-to-ground fault with the fault resistance of 3 Ω occurs at bus 6 of the DCMG, and it remains for a period of 0.05 s. During this time period, the charging current of EV_1 is −130 A. As shown in Fig. 15(a), if the EV charger is controlled by the CC method with SC support, the DC-bus voltage drops by 6%, which reaches the maximum permitted voltage drop according to the standard of Australian Renewable Energy Agency [30]. At $t=1.55$ s, when the fault is cleared, the DC-bus voltage experiences an 8.5% overshoot that exceeds the standard limit 6%.

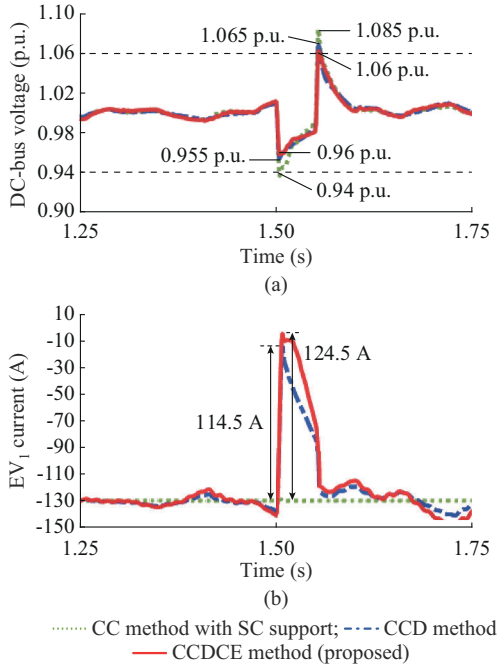

Fig. 15. Case study B: performance of system during a line-to-ground fault. (a) DC-bus voltage. (b) EV_1 current.

However, if the voltage supportive methods (the CCD method and the proposed CCDCE method) are used, since lower power is taken by the EV during the fault (Fig. 15(b)), the undershoot and overshoot of the DC-bus voltage maintain within the standard limit 6%, as shown in Fig. 15(a). The undershoot and overshoot using CCD method are 4.5%

and 6.5%, respectively, while those using the proposed CCDCE method are 4% and 6%, respectively. This case study validates the ability of the software-based solutions (CCD and CCDCE methods) in supporting the DC-bus voltage, while also showing the stronger performance of the proposed CCDCE method compared with CCD method.

C. Case Study C: Ultra-fast Charging of Three EVs

In this case study, a whole EV charging station including three individual ultra-fast chargers is simulated and the performances of the three control methods are compared. This case study investigates the dynamic responses of the CC method with SC support, CCD method, and the proposed CCDCE method, while one EV, two EVs, and three EVs connect/disconnect at different time intervals.

At $t=0.5$ s, EV_1 starts charging with the current of $I_{EV}^{*}=-130$ A, and then stops charging at $t=3$ s. EV_1 is charging from $t=0.5$ to $t=3$ s, EV_2 starts charging at $t=1$ s and then stops at $t=2.5$ s, and EV_3 starts charging at $t=1.5$ s and then stops at $t=2$ s. As can be observed in Fig. 16(a), the connection and disconnection of EV_1, EV_2, and EV_3 cause some overshoots/undershoots on the DC-bus voltage, which are different in magnitudes using different control methods.

In Fig. 16(a), the undershoot of the DC-bus voltage caused by charging of one EV (EV_1) at $t=0.5$ s is similar to the results shown in case study A. At $t=1$ s, when the second EV (EV_2) is added, if the CC method with SC support is used for charging of both EVs, the DC-bus voltage experiences a 5% undershoot. It should be noted that using the CC method with SC support, both EVs act as static loads for the DCMG as they just demand power from the DC bus without having support on regulating the DC-bus voltage. However, if the CCD and CCDCE methods are used, both EVs become static bus voltage supportive loads and dynamic bus voltage supportive loads, respectively. As a result, the undershoots of the DC-bus voltage decrease to 2% and 1%, respectively, as shown in Fig. 16(a). The dynamics of charging currents for EV_1 and EV_2 using different control methods are shown in Fig. 16(b) and (c), respectively. At $t=1$ s, the variation of the charging current for EV_1 is 26 A if the proposed CCDCE method is used, followed by 40 A if the CCD method is used.

At $t=1.5$ s when the third EV (EV_3) is added, the DC-bus voltage experiences its maximum undershoot (6%) while the CC method with SC support is used. Whereas, the undershoots on the DC-bus voltage are minimum at 1% and 0.5%, respectively, while using the CCD and CCDCE methods. This validates better results with more voltage-supportive EV chargers connected to the grid.

At $t=2$ s, when EV_3 stops charging, an overshoot appears on the DC-bus voltage, as shown in Fig. 16(a). Using the CCDCE and CCD methods, the overshoots on the DC-bus voltage are 0.4% and 1%, respectively, and the overshoot is 4% when the CC method with SC support is used. Similarly, when EV_2 and EV_1 stop charging at $t=2.5$ s and at $t=3$ s, respectively, the proposed CCDCE method exhibits the lowest overshoot on the DC-bus voltage compared with the other two methods. According to the results of this test, the proposed CCDCE method exhibits an improved dynamic response compared with the other two methods during different charging scenarios in a charging station.

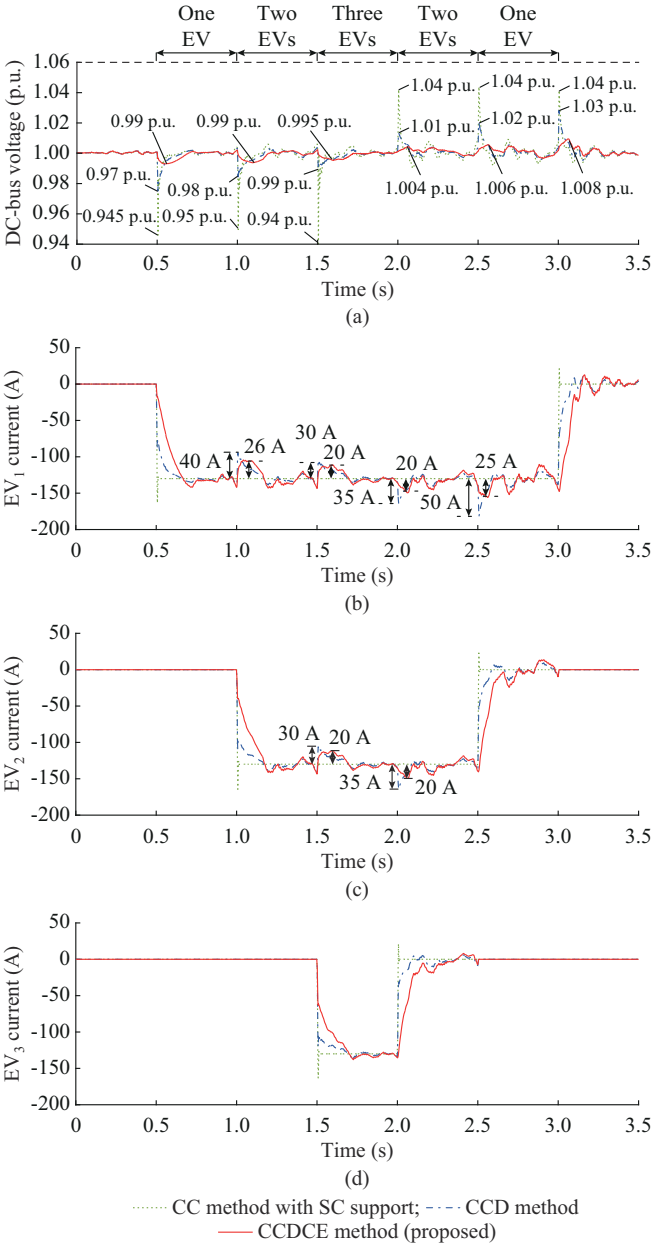

Fig. 16. Case study C: dynamic responses while one EV, two EVs, and three EVs connect and disconnect at different time intervals. (a) DC-bus voltage. (b) EV_1 current. (c) EV_2 current. (d) EV_3 current.

As shown in the presented results, although the charging current slightly changes during both the ultra-fast charging and the line-to-ground fault to support the DC-bus voltage, this variation occurs during a very short time period (≈ 0.5 s), which is negligible and does not have any noticeable impact on the charging efficiency.

VI. Conclusion

A control method based on the idea of emulating a supercapacitor is proposed for ultra-fast EV charging operation in an islanded DCMG. Unlike the conventional constant charg-

ing current method and the *P/V* droop-based control method, the proposed method turns the EV into a dynamic bus voltage supportive load for the DCMG. As a result, the undershoot/overshoot of the DC-bus voltage caused by the ultra-fast charging process are reduced without enlarging and complicating the hardware of the charging station. The proposed control method exhibits high robustness and better performance against severe disturbances. A detailed design guideline is presented for the conventional as well as the proposed methods, and the performances of the three methods are compared using different case scenarios. The results show that the proposed control method can be an effective and reliable alternative for EV chargers in charging stations of islanded DCMGs. A future work to continue this research would be to experimentally implement the proposed controller in a real islanded DCMG.

REFERENCES

[1] W. Su, H. Eichi, W. Zeng *et al.*, "A survey on the electrification of transportation in a smart grid environment," *IEEE Transactions on Industrial Informatics*, vol. 8, no. 1, pp. 1-10, Oct. 2011.

[2] A. Ahmadian, B. Mohammadi-Ivatloo, and A. Elkamel, "A review on plug-in electric vehicles: introduction, current status, and load modeling techniques," *Journal of Modern Power Systems and Clean Energy*, vol. 8, no. 3, pp. 412-425, Jan. 2020.

[3] B. J. Birt, G. R. Newsham, I. Beausoleil-Morrison *et al.*, "Disaggregating categories of electrical energy end-use from whole-house hourly data," *Energy and Buildings*, vol. 50, pp. 93-102, Jul. 2012.

[4] S. Deilami, A. S. Masoum, P. S. Moses *et al.*, "Real-time coordination of plug-in electric vehicle charging in smart grids to minimize power losses and improve voltage profile," *IEEE Transactions on Smart Grid*, vol. 2, no. 3, pp. 456-467, Aug. 2011.

[5] R. A. Biroon, Z. Abdollahi, and R. Hadidi, "Fast and regular electric vehicle charging impacts on the distribution feeders," in *Proceedings of 2019 IEEE Industry Applications Society Annual Meeting*, Baltimore, USA, Oct. 2019, pp. 1-7.

[6] A. Alsabbagh, H. Yin, and C. Ma, "Distributed electric vehicles charging management with social contribution concept," *IEEE Transactions on Industrial Informatics*, vol. 16, no. 5, pp. 3483-3492, Oct. 2019.

[7] A. Lucas, F. Bonavitacola, E. Kotsakis *et al.*, "Grid harmonic impact of multiple electric vehicle fast charging," *Electric Power Systems Research*, vol. 127, pp. 13-21, Oct. 2015.

[8] B. Alharbi and D. Jayaweera, "Impact assessment of plug-in electric vehicle charging locations on power systems with integrated wind farms incorporating dynamic thermal limits," *Journal of Modern Power Systems and Clean Energy*, vol. 10, no. 3, pp. 710-718, May 2021.

[9] R. Crosier, S. Wang, and M. Jamshidi, "A 4800-V grid-connected electric vehicle charging station that provides STACOM-APF functions with a bi-directional, multi-level, cascaded converter," in *Proceedings of 2012 Twenty-Seventh Annual IEEE Applied Power Electronics Conference and Exposition (APEC)*, Orlando, USA, Feb. 2012, pp. 1508-1515.

[10] Y. Liu, Y. Tang, J. Shi *et al.*, "Application of small-sized SMES in an EV charging station with DC bus and PV system," *IEEE Transactions on Applied Superconductivity*, vol. 25, no. 3, pp. 1-6, Nov. 2014.

[11] T. Dragičević, S. Sučić, J. C. Vasquez *et al.*, "Flywheel-based distributed bus signalling strategy for the public fast charging station," *IEEE Transactions on Smart Grid*, vol. 5, no. 6, pp. 2825-2835, Jun. 2014.

[12] K.-W. Hu and C.-M. Liaw, "Incorporated operation control of DC microgrid and electric vehicle," *IEEE Transactions on Industrial Electronics*, vol. 63, no. 1, pp. 202-215, Sept. 2015.

[13] S. Bai and S. M. Lukic, "Unified active filter and energy storage system for an mw electric vehicle charging station," *IEEE Transactions on Power Electronics*, vol. 28, no. 12, pp. 5793-5803, Mar. 2013.

[14] S. Taghizadeh, M. Karimi-Ghartemani, M. J. Hossain *et al.*, "A fast and robust DC-bus voltage control method for single-phase voltage-source DC/AC converters," *IEEE Transactions on Power Electronics*, vol. 34, no. 9, pp. 9202-9212, Nov. 2018.

[15] H. Hõimoja, A. Rufer, G. Dziechciaruk *et al.*, "An ultrafast EV charging station demonstrator," in *Proceedings of International Symposium on Power Electronics Power Electronics, Electrical Drives, Automation and Motion*, Sorrento, Italy, Jun. 2012, pp. 1390-1395.

[16] P. Mitra and G. Venayagamoorthy, "Wide area control for improving stability of a power system with plug-in electric vehicles," *IET generation, Transmission & Distribution*, vol. 4, no. 10, pp. 1151-1163, Oct. 2010.

[17] J. Y. Yong, V. K. Ramachandaramurthy, K. M. Tan *et al.*, "Bi-directional electric vehicle fast charging station with novel reactive power compensation for voltage regulation," *International Journal of Electrical Power & Energy Systems*, vol. 64, pp. 300-310, Jan. 2015.

[18] M. C. Kisacikoglu, M. Kesler, and L. M. Tolbert, "Single-phase on-board bidirectional PEV charger for V2G reactive power operation," *IEEE Transactions on Smart Grid*, vol. 6, no. 2, pp. 767-775, Oct. 2014.

[19] S. Dinkhah, C. A. Negri, M. He *et al.*, "V2G for reliable microgrid operations: voltage/frequency regulation with virtual inertia emulation," in *Proceedings of 2019 IEEE Transportation Electrification Conference and Expo (ITEC)*, Detroit, USA, Jun. 2019, pp. 1-6.

[20] M. Mazumder and S. Debbarma, "EV charging stations with a provision of V2G and voltage support in a distribution network," *IEEE Systems Journal*, vol. 15, no. 1, pp. 662-671, Jul. 2020.

[21] D. Xu, A. Xu, C. Yang *et al.*, "Uniform state-of-charge control strategy for plug-and-play electric vehicle in super-UPS," *IEEE Transactions on Transportation Electrification*, vol. 5, no. 4, pp. 1145-1154, Sept. 2019.

[22] J. Li, Q. Yang, F. Robinson *et al.*, "Design and test of a new droop control algorithm for a SMES/battery hybrid energy storage system," *Energy*, vol. 118, pp. 1110-1122, Jan. 2017.

[23] N. Poursafar, S. Taghizadeh, M. J. Hossain *et al.*, "An optimized distributed cooperative control to improve the charging performance of battery energy storage in a multiphotovoltaic islanded DC microgrid," *IEEE Systems Journal*, vol. 16, no. 1, pp. 1170-1181, May 2021.

[24] N. L. Diaz, T. Dragičević, J. C. Vasquez *et al.*, "Intelligent distributed generation and storage units for DC microgrids – a new concept on cooperative control without communications beyond droop control," *IEEE Transactions on Smart Grid*, vol. 5, no. 5, pp. 2476-2485, Aug. 2014.

[25] M. A. Elgendy, B. Zahawi, and D. J. Atkinson, "Assessment of perturb and observe MPPT algorithm implementation techniques for PV pumping applications," *IEEE Transactions on Sustainable Energy*, vol. 3, no. 1, pp. 21-33, Dec. 2011.

[26] M. Karimi-Ghartemani, S. Khajehoddin, P. Jain *et al.*, "Linear quadratic output tracking and disturbance rejection," *International Journal of Control*, vol. 84, no. 8, pp. 1442-1449, Aug. 2011.

[27] J. C. Vasquez, J. M. Guerrero, A. Luna *et al.*, "Adaptive droop control applied to voltage-source inverters operating in grid-connected and islanded modes," *IEEE Transactions on Industrial Electronics*, vol. 56, no. 10, pp. 4088-4096, Jul. 2009.

[28] J. Jiang, Q. Liu, C. Zhang *et al.*, "Evaluation of acceptable charging current of power Li-ion batteries based on polarization characteristics," *IEEE Transactions on Industrial Electronics*, vol. 61, no. 12, pp. 6844-6851, Apr. 2014.

[29] S. Dey, Z. A. Biron, S. Tatipamula *et al.*, "Model-based real-time thermal fault diagnosis of Lithium-ion batteries," *Control Engineering Practice*, vol. 56, pp. 37-48, Nov. 2016.

[30] B. Noone. (2013, Sept.). PV integration on australian distribution networks: literature review. [Online]. Available: https://www.ceem.unsw.edu.au

[31] M. A. H. Rafi and J. Bauman, "A comprehensive review of DC fast-charging stations with energy storage: architectures, power converters, and analysis," *IEEE Transactions on Transportation Electrification*, vol. 7, no. 2, pp. 345-368, Aug. 2020.

Noushin Poursafar received the M.Res and Ph.D. degrees in electrical engineering from Macquarie University, Sydney, Australia, in 2018 and 2022, respectively. Her research interests include electric vehicle chargers, microgrid, renewable energy integration, and power system stability and control.

Seyedfoad Taghizadeh received the Ph.D. degree in electrical engineering from the Macquarie University, Sydney, Australia, in 2018. He is currently working as a Lecturer in the School of Engineering, Macquarie University. His research interests include electric vehicle chargers, control systems, renewable energy integration, power quality, and energy storage systems.

M. Jahangir Hossain received the B.Sc. and M.Sc. Eng. degrees from Ra-

jshahi University of Engineering and Technology (RUET), Rajshahi, Bangladesh, in 2001 and 2005, respectively, and the Ph.D. degree from the University of New South Wales, Sydney, Australia, in 2010, all in electrical and electronic engineering. He is currently an Associate Professor with the School of Electrical and Data Engineering, University of Technology, Sydney, Australia. Before joining there, he served as an Associate Professor in the School of Engineering, Macquarie University, Sydney, Australia, Senior Lecturer and a Lecturer in the Griffith School of Engineering, Griffith University, Brisbane, Australia, for five years and as a Research Fellow in the School of Information Technology and Electrical Engineering, University of Queensland, Brisbane, Australia. His research interests include renewable energy integration and stabilization, voltage stability, microgrids and smart grids, robust control, electric vehicles, building energy management systems, and energy storage systems.

Masoud Karimi-Ghartemani received the Ph. D. degree in electrical and computer engineering from University of Toronto, Toronto, Canada, in 2004. From 2005 to 2008, he was a Faculty Member with the Department of Electrical Engineering, Sharif University of Technology, Tehran, Iran. From 2008 to 2011, he was a Member of the ePOWER Laboratory, Queen's University, Kingston, Canada. Since 2012, he has been with the Department of Electrical and Computer Engineering (ECE), Mississippi State University (MSU), Mississippi, USA, where he is currently a Professor. His teaches courses in control systems and energy systems. He works on modeling, control, and operation of distributed energy systems at high penetration level. He is the recipient of the 2020 Faculty Research Award at MSU's Bagley College of Engineering, and Teaching Excellence at ECE Department . He is an Associate Editor for the IEEE Transactions on Industrial Electronics, IEEE Transactions on Sustainable Energy, and IEEE PES Letters. His particular research interests include integration of distributed and renewable energy systems.